Neoteric Semi-embedded β-tricalcium Phosphate Promotes Osteogenic Differentiation of MSCs under Cyclic Stretch

Yujie Dai[a, b], *Qingyun Xie*[c], *Yimeng Zhang*[a], *Yiwan Sun*[a], *Shaomei Zhu*[a], *Chongyu Wang*[a], *Youhua Tan*[d, e], *Xue Gou*[a, b, *]

[a] Institute of Biomedical Engineering, College of Medicine, Southwest Jiaotong University, Chengdu 610031, P.R. China
[b] Key Laboratory of Advanced Technologies of Materials, Ministry of Education, School of Materials Science and Engineering, Southwest Jiaotong University, Chengdu 610031, P.R. China
[c] Department of Orthopedics, General Hospital of Western Theater Command, Chengdu 610031, China
[d] The Hong Kong Polytechnic University Shenzhen Research Institute, Shenzhen (518000), China
[e] Department of Biomedical Engineering, The Hong Kong Polytechnic University, Hong Kong (999077), China

Keywords: Cell adhesion; Intracellular calcium signals; Osteogenic differentiation; Piezo signaling pathway; Uniaxial cyclic stretching

Graphical abstract

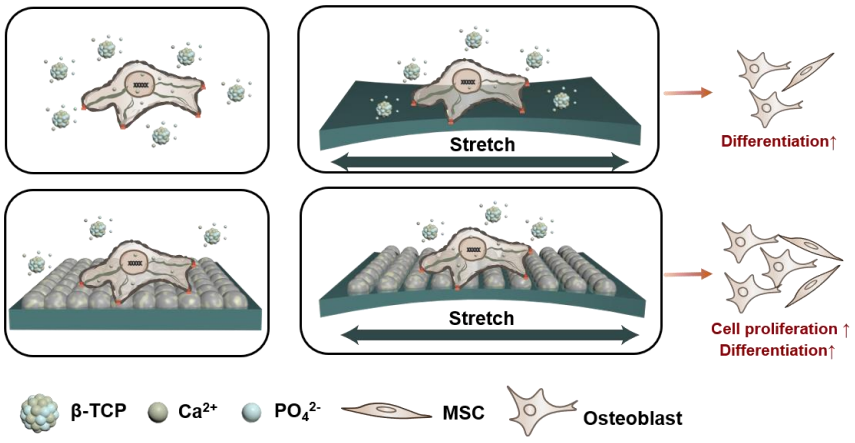

Abstract

β-tricalcium phosphate (β-TCP) is a bioactive material for bone regeneration, but its brittleness limits its use as a standalone scaffold. Therefore, continuous efforts are necessary to effectively integrate β-TCP into polymers, facilitating a sturdy ion exchange for cell regulation. Herein, a novel semi-embedded technique was utilized to anchor β-TCP nanoparticles onto the surface of the elastic polymer, followed by hydrophilic modification with the polymerization of dopamine. Cell adhesion and osteogenic differentiation of mesenchymal stem cells (MSCs) under static and dynamic uniaxial cyclic stretching conditions were investigated. The results showed that the new strategy was effective in promoting cell adhesion, proliferation and osteogenic induction by the sustained release of Ca^{2+} in the vicinity, and creating a reasonable roughness. Specifically, the released Ca^{2+} from β-TCP could activate the calcium signaling pathway, which further upregulated Calmodulin and Calcium/calmodulin-dependent protein kinase II genes in MSCs. Meanwhile, the roughness of the membrane and the uniaxial cyclic stretching activated the PIEZO1 signaling pathway. Chemical and mechanical stimulation promotes osteogenic differentiation and increases the expression of related genes 2-8 fold. These findings demonstrated that the neoteric semi-embedded structure was a promising strategy in controlling both chemical and mechanical factors of biomaterials for cell regulation.

1. Introduction

β-tricalcium phosphate (β-TCP), classified as a bioactive ceramic material, is widely employed as an artificial bone substitute in the clinical area due to its excellent osteotransductivity, osteoinductivity, biodegradability, and similar chemical composition to bone[1]. Once implanted *in vivo*, the degraded calcium (Ca) and inorganic phosphate (P) from β-TCP can enter the living circulatory system to regulate cell behavior and promote the formation of new bones. Nevertheless, the chemical composition of β-TCP is not the sole determinant of its bioactivity. Many studies have demonstrated various structure characteristics, including particle size, roughness, stiffness and porosity, significantly influence the bone regenerative potential of β-TCP[2]. Despite these progresses, the bone regenerative performance of β-TCP scaffolds is generally still considered to be inferior to that of autologous bone. Therefore, conducting thorough research on material design optimization and elucidation of the specific role that each property plays in the biological response is critical for the development of more effective bone graft substitutes.

Currently, β-TCP has been utilized for bone regeneration in the forms of scaffold implant, bone cement, and coating. Specifically, the limitation of using β-TCP alone is that it does not exhibit good mechanical properties and is prone to fragile failure[3]. Efforts have been made to combine bioactive ceramics with polymers to improve their performance. For example, β-TCP nanoparticles, which possess a high surface-to-volume ratio and a specific proteome adhesion to enhance osteogenesis, were sintered with polyetheretherketone and poly-L-lactic acid to form a multi-material scaffold[4]. The scaffold exhibited excellent mechanical strength and enabled the contact of β-TCP with the body fluid through degradation of poly-L-lactic acid, benefiting ion-exchange

and new bone formation. However, in these studies, β-TCP nanoparticles were usually encapsulated in polymeric materials by sintering[5,6]. The release of Ca and P would be hindered if β-TCP was wrapped by materials with low degradability or is non-degradable, blocking their intended bone repair effect. Conversely, while the encapsulating material is degraded rapidly, β-TCP will be released into body fluid as free nanoparticles during the degradation. These liberated particles can either be carried away through fluid transport or accumulate in specific regions to damage organelles such as lysosomes, mitochondria, endoplasmic reticulum, and affect normal cellular metabolism[7]. Poor discussion have been made on how to effectively add β-TCP to the substrate while exploring the regulatory role of cells in dynamic environments. Thus, ongoing efforts are required to successfully incorporate β-TCP into polymers, enabling the formation of continuous ion exchange and fostering the process of bone repair.

In addition, growing evidence has demonstrated that a comprehensive understanding of cell regulatory mechanisms is indispensable for attaining the optimal design of materials[8]. Traditional research, which investigated cell-material interaction in a static environment *in vitro*, was valuable in refining biomaterial design. However, there have been instances where the results obtained *in vitro* do not align with the outcomes observed during actual implantation in living organisms. Biomaterials implanted *in vivo* will be subjected to mechanical stimulation including tension, compression, and fluid shear. Therefore, researchers believe that studying how cells behave on biomaterials in dynamic environments is an effective strategy for further improving material design. Among the various mechanical stimuli, the dynamic strain generated by tensile loading on the material has been proven to effectively regulate cell adhesion and stimulate osteogenic differentiation of MSCs. For instance, Wu et al. found that 1 h of stretching could lead to the activation of a calcium-responsive mechanosensitive channel, resulting in concentrated cellular actin fibers[9]. Lei et al. studied the effect of various strains and frequencies on MSCs differentiation, and concluded that using uniaxial cyclic stretching (UCS) with 10% strain at the frequency of 1 Hz could enhance the expression of osteogenic genes in MSCs, such as Alkaline phosphatase (*Alp*), Bone morphogenetic protein-2 (*Bmp2*) and Runt-related transcription factor 2 (*Runx2*)[10]. Although cells in natural bone tissue experience microstrains far below 10% imposed by the substrate, studies have demonstrated that MSCs previously stimulated by mechanical loading *in vitro* before implantation have mechanical memory, which could contribute to bone formation and accelerate bone healing *in vivo*[11]. Therefore, the construction of a dynamically stretching environment *in vitro* is conducive to further optimizing material design and regulating the behavior of cells on biomaterials, thus promoting dynamic tissue repair *in vivo*.

To accomplish the objective of the study, i.e., establishing a sustainable β-TCP interface for MSCs regulation and understanding the influences of chemical and structural characteristics of β-TCP on cell regulation mechanisms both in static and dynamic microenvironments, a neoteric semi-embedded method was employed to immobilize β-TCP nanoparticles on semi-cured elastic polymer (polydimethylsiloxane, PDMS). Additionally, polydopamine[12,13], which is widely used as a surface modification material due to its excellent biocompatibility and chemical stability, have

been used to improve the hydrophilicity of the substrate. The stability of the material was investigated in the form of morphology and roughness change as well as weight loss and Ca^{2+} release. In addition, cytocompatibility was determined by exploring cell behaviors, including adhesion, proliferation, and differentiation in static conditions and UCS (10% strain, 1 Hz). Moreover, real-time quantitative polymerase chain reaction (RT-qPCR) was implemented to decouple the roles of chemical stimulation, roughness and dynamic tensile strain in osteogenic differentiation of MSCs.

2. Materials and Methods

2.1 Preparation of Membranes

PDMS elastomer substrates were combined with a cross-linker (Sylgard 184, dow corning) at 70℃ for 15 min (semi-solid PDMS). β-TCP dispersing solution was separately made by combining 20, 40, and 60 mg of β-TCP nanoparticles (Apri, China) in 10 mL of absolute ethyl alcohol with sonicating. Semi-solid PDMS was fully coated with β-TCP dispersing solution at 60°C until the PDMS solidified and the alcohol evaporated completely (samples named as eβT). Then, according to a prior study[13], eβT was hydrophilically modified by immersing it in the 10 mM Tris-HCL buffer at pH 8.5 overnight for dopamine, resulting in sample fabrication of eβP.

2.2 Characterization of Membranes

Before being observed, specimens cut into 1×1 cm^2 were coated with a 15 nm Au layer using rotary-pumped sputter coating (EM ACE200, Leica, Germany). Samples were imaged with the scanning electron microscope (SEM, Merlin Gemini II, Zeiss, USA) using a SE detector, applying a voltage of 3 kV, and a working distance of 8-12 mm.

The membranes' surface topography features and surface roughness were characterized by an atomic force microscope (AFM, Moltimode 8, Bruker, USA) operating in tapping mode in the air. The average roughness (RA) was analyzed by Nanoscope analysis software.

The water contact angle was measured using DSA100 (Kruss, Germany) to assess hydrophilicity. The average contact angle values were determined from at least five observations per sample.

X-ray diffraction (XRD, Panalytical Empyrean 2, France) was used to analyze phase compositions collected in the 10-70° range with a knife spacing of 1 mm, angular interval of 0.02, and a time step of 0.5 s.

Fourier transform infrared spectrometer (FTIR, Themos Nicolet 5700, USA) was used to detect chemical bonds in molecules with a wavenumber range of 4000-650 cm^{-1} and a resolution of 4 cm^{-1}.

2.3 Biodegradability of eβP

eβP films were cut into 10×30 mm^2 and completely submerged in 20 mL ddH_2O (Southwest Jiaotong University, China) in a shaker at 80 rpm at 37℃ for up to 7 days (1, 3, 5, 7). At the end of each incubation period, membranes were carefully extracted from ddH_2O, rinsed with distilled water to remove the ions absorbed on the membrane surface, and weighed after being completely dried. The weight loss was determined using the formula: Weight loss (%) = (W0-W1)/W0 × 100%, where W0 and W1 were the scaffold dry weights before and after immersion, respectively[4]. The eβP film and nano β-TCP

particles (0.1 mg/mL) were separately immersed in ddH_2O, then shaken at 80 rpm in a thermostat shaker at 37°C. At predetermined time points, changes in cumulative ion concentrations were monitored by atomic absorption spectrometer (PinAAcle 900T PerkinElmer, USA), respectively.

2.4 Material Stability Testing

The coherence and adherence of the β-TCP layers were tested by embedding a nano β-TCP coating in the middle of two pre-prepared semi-cured PDMS, and evaluating the bonding ability of the coating to the substrate material by increasing the tensile force until the coating was peeled off from the substrate[14].

Friction and wear tests were conducted using a high-speed friction and wear tester (MFT-R4000, TakTark, China). The applied load was 10 N, sliding time was 20 min, sliding distance was 5 mm, and frequency was 1 Hz.

The eβP films were cut into 10 × 30 mm^2 and loaded with a homemade uniaxial cyclic tensile machine[15] at 1 hz 10% strain for 1 h, to characterize the change of their morphology with SEM. Samples were completely immersed in 20 ml of ddH_2O in a shaker at 37 °C, 80 rpm for 1 day to characterize the Ca and P elemental release (iCAP TQs, ICP-MS, Thermo, Germany).

2.5 Material Sterilization and Cell Culture

Before the experiment, 10×30 mm^2 of PDMS and eβP were cut. PDMS, eβP, and nanoparticles β-TCP were fixed in steam for 30 min at 121°C under 103 kPa pressure. MSCs were purchased from Saiy Biological Technology Co., Ltd. (China). MSCs were cultured with a complete medium containing α-MeM medium (Gibco, USA), 10% fetal bovine serum (Gibco, USA), and 1% penicillin/streptomycin with 5% CO_2 in a humidified atmosphere. Nano β-TCP particles were mixed with a complete culture medium at a final ratio of 0.1 mg/mL in the nβT group. 5×10^5 cells/mL were separately inoculated in each group cultured in complete medium, and the medium was refreshed every two days.

2.6 Dynamic Culturing of MSCs Under UCS

MSCs were inoculated at a concentration of 5×10^5 cells/mL on PDMS, and eβP for 12 h. Then, the samples were placed in a homemade uniaxial cyclic tensile machine[15] and put in the incubator with the oxygen content of 5% and a temperature of 37°C. Each sample was given a tensile loading with 10% strain in amplitude and 1 Hz in frequency for 1 h. These experimental groups were named SPDMS and SeβP, respectively. In addition, 0.1 mg/mL of nano β-TCP particles were added into cells cultured on PDMS, and dynamically cultured, which was named as SnβT group.

2.7 Cell Viability and Cell Proliferation

Cell viability was tested using Fluorescein diacetate (Sigma, USA, 20 mM) and Propidium iodide (Sigma, USA, 10 mM) solutions for 30 min after 1 day of culture. The stained samples were examined using an IX 83 microscope (Olympus, Japan).

Cell proliferation was measured using CCK-8 (C0037, Beyotime Biotechnology, China) at day 1, 3, 5, and 7, and the absorbance was measured at 450 nm. The well plate group was used as the control. In addition, cell proliferation was determined with the YF® 488 Click-it EdU imaging kit (EdU C6015, UElandy, China) after 1 day of culture. Cells were incubated with 10 μM EdU for 12 h at 37°C. Then, MSCs were fixed in 4%

paraformaldehyde solution for 10 min and rinsed with phosphate-buffered saline (PBS). After permeabilization with 0.1% Triton X-100 for 5 min and rinsing with PBS, MSCs were exposed to 500 μL Click-it working solution for 30 min, followed by incubation with Hoechst 33342 (H4079, UElandy, China) working solution for 15 min to stain nuclear. Images were captured using 495 nm excitation and 519 nm emission by IX 83. The percentage of EdU-positive cells was defined as the proliferation rate.

2.8 Cell morphology and Cell Adhesion

After 1 day of culture, cells were fixed with 4% paraformaldehyde for 30 min and washed 3 times with PBS. Thereafter, the cells were permeabilized by 0.5% Triton X-100 followed by blocking with 5% bovine serum albumin (BSA) solutions for 15 min and washed 3 times with PBS. Cells were then closed with 3% BSA prepared in PBS for 1 h. Subsequently, the staining was performed under light-proof conditions. Vinculin (Invitrogen, USA) was diluted with 3% BSA to a concentration of 10 μg/mL, and 100 nM of Phalloidin-Alexa Fluor 488 (Invitrogen, USA) was diluted in PBS. Cells were incubated for 30 min at 37°C and washed three times with PBS for 5 min. Finally, 4',6-Diamidino-2-phenylindole dihydrochloride (DAPI, Beyotime, China) was diluted with pbs to 5 μg/mL, stained for 5 min at room temperature and protected from light. After being washed three times with PBS, cells were imaged and photographed using IX 83.

2.9 Immunofluorescent staining

Cells in the PDMS group were cultured for up to 3 days with the Mouse Bone Marrow MSC Osteogenic Differentiation Kit (MUXMX-90021, OriCell, China) and labeled as PDMS+, while the other groups were cultured for 3 days with normal complete medium. Cells were fixed with 4 % paraformaldehyde, permeabilized with 0.5 % Triton X-100 in PBS for 15 min, and then blocked with 3 % BSA for 1 hour. Antibodies used for immunofluorescence staining were rabbit BMP-2 antibody at 1:200 dilution (Abclonal, China) and rabbit RUNX2 antibody at 1:200 dilution (MCE, China) incubated at 4°C for 12 h. The cells were washed with PBS and incubated for 1 h. The cells were then incubated with 0.5 % Triton X-100 in PBS for 15 min. After rinsing with PBS, cells were incubated with fluorophore-conjugated secondary antibodies (Cy3 goat anti-rabbit IgG (H + L) or FITC goat anti-rabbit IgG (H + L) (Abclonal, China)) for 1 h at room temperature. After rinsing with PBS again, the nuclei were counterstained with 4',6-diamidino-2-phenylindole, and the cytoskeleton was stained with the flavonoid Phalloidin-Alexa Fluor 488/594 (Invitrogen, USA) and then imaged using FM.

2.10 Osteogenic differentiation assay on MSCs

Cells were cultured in different groups for up to 8 days (2, 4, 6, 8). ALP was measured using the BCIP/NBT kit (C3206, Beyotime, China), and images were taken under a light microscope. Grayscale values of the ALP protein were measured using ImageJ. Similarly, osteoblast mineralized nodules were detected using the Osteoblast Mineralized Nodules Staining kit (C0148, Beyotime, China) for each group. The nodules were fixed, stained with alizarin red s (ARS). Then, absorbance at 450 nm was measured using an enzyme meter and photographed under a microscope. In addition, ARS after 14 days of culture were measured.

2.11 Real-time quantitative polymerase chain reaction

Trizol reagent (Invitrogen, USA) was used to extract the total RNA from each batch

of MSCs in accordance with the manufacturer's instructions. The quality and quantity of total RNA were measured using a nano-300 spectrophotometer with a 260/280 absorbance ratio. The Exon SCRIPT RT SuperMix with dsDNase cDNA synthesis kit (A502, Exonart, China) was used for reverse transcription. Real-time Q-PCR was carried out in a volume containing 10 L of the 2x FastSYBR Green qPCR Master Mix UDG, 0.2 M of the upper and lower primers, 50 ng of cDNA, and a volume of 20 L of RNase-free RNase water template. 50 ng of cDNA and water without RNase. CFX-linked real-time PCR detection system (Bio-RAD, USA) was used to carry out the reactions. The amplification profile used was 5 min at 95°C, 40 cycles at 95°C for 5 s, and 40 cycles at 65° for 20 s. The amplification profile used for the reactions was 5 min at 95°C, 40 cycles at 95°C for 5 s, and 40 cycles at 65° for 20 s using a CFX-linked real-time PCR detection system. Using the gene-specific primer pairs in Table 1, the quantitative expressions of the target mRNAs were determined.

Table 1. Quantitative expressions of target mRNAs were determined using gene-specific primer pairs.

Gene target	Primer sequence	
	Forward	**Reverse**
Cam	CAGCAGCCAACCTTTCACCC	CCACCTAGTTCATCAAAGCCACC
Gapdh	GGACCAGGTTGTCTCCTGTG	CATTGAGAGCAATGCCAGCC
Alp	ATCTTTGGTCTGGCTCCCATG	TTTCCCGTTCACCGTCCAC
Runx2	ACCAGCAGCACTCCATATCTCTAC	CTTCCATCAGCGTCAACACCATC
Piezo1	TGCCTCAGCCTCCTCTTC	CTTCAGGTCCAGCCTTGTA
Col1a	ACAGACGAACAACCCAAACT	GGTTTTTGGTCACGTTCAGT
Bmp2	GAGGAGAAGCCAGGTGTCT	GTCCACATACAAAGGGTGC
Camk2	CGGTCTACGGTGGCATCCAT	CTTGGGCTGGGCTTACGAGA

2.12 Statistical Analysis

All quantitative data were expressed as mean±standard deviation. Statistical analyses were performed using Graphpad Prism 9.0 software. Statistical differences were determined using one-way ANOVA and two-way ANOVA. The abc marker method identified significant differences between groups by comparing mean values. The group with the highest mean was labeled "a", and if the difference with the second-highest group was significant, that group was labeled "b". If not, the comparison was made with the third group. The cycle continued until the group with the smallest mean was labeled.

3. Results and Discussion

3.1 Fabrication and Characterization of eβP

Figure 1A illustrated the process for creating the semi-embedded β-TCP membrane which featured a nanomorphology and the degradation of β-TCP. The PDMS films were partially cured and further covered by ultrasound-treated homogeneous nano-β-TCP (500 nm β-TCP nanoparticles) suspensions. Then, the samples were heated at 70°C until fully cured. Such a semi-embedded design avoided the complete encapsulation of β-TCP by PDMS, which led to the inability of nano-β-TCP to degrade and release Ca^{2+} and PO_4^{3-} [5]. First, β-TCP nanoparticles were characterized using SEM imaging and

semiquantitative EDS elemental analysis (Figure S1). The elements Ca and P were detected. In addition, the XRD patterns of nano-β-TCP were consistent with the standard spectrum of β-TCP (JCPDF 09-0169). Then, the amount of β-TCP utilized in sample fabrication was optimized. SEM morphological characterization in Figure 1B depicted that using 20 mg of β-TCP (eβT$_{20}$), resulted in incomplete coverage of the sample's surface, leading to the presence of more empty spaces or voids. In comparison, when using 40 mg (eβT$_{40}$) and 60 mg (eβT$_{60}$) of β-TCP, the surface of the film was completely covered with nanoparticles. As more amount of nanoparticles may contribute to increased agglomeration, which may lead to the formation of cracks during mechanical loading[16] , thus 40 mg was utilized for sample (named eβT) fabrication in the following study. Furthermore, the sample was subjected to PDA for a period of 12 h to improve the hydrophilicity based on our previous studies[13]. The modified samples were named as eβP.

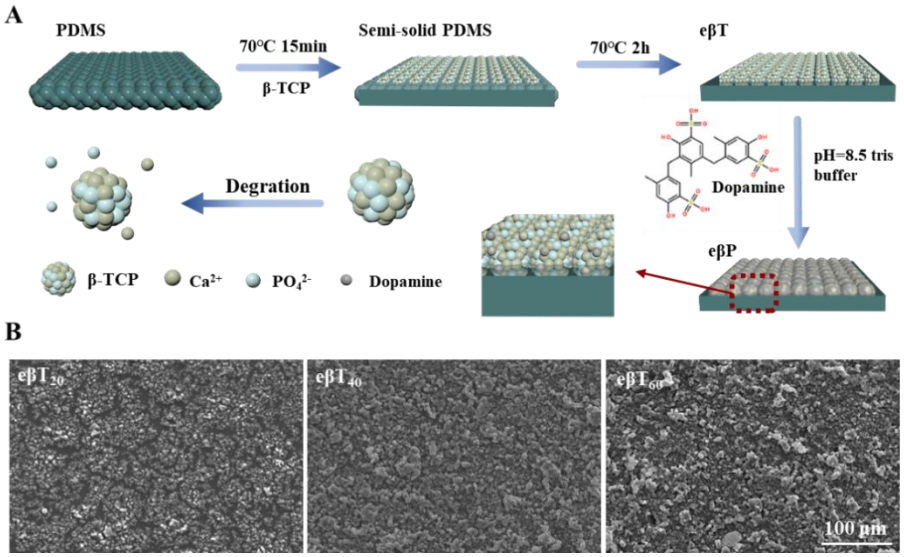

Figure 1. Fabrication and optimization of eβP. (A) The schematic diagrams for the fabrication of eβP. (B) The SEM morphological characterization of eβT$_{20}$, eβT$_{40}$ and eβT$_{60}$.

Figure 2A showed the SEM micrographs of eβT and eβP, indicating that nano-β-TCP was uniformly embedded at the elastic membrane surface. The average embedding depth of eβT and eβP, was around 7.12 and 7.45 μm, respectively. In addition, AFM tests suggested that the surface roughness of eβP (386±83 RA) was slightly reduced compared to eβT (466±77 RA) due to the attachment of PDA in the spaces between the particles (Figure 2B). The formation of PDA could further improve the hydrophilicity of the sample, and reduce the water contact angles from 126.4±2.2° for eβT to 86.7±1.5 for eβP, making the samples more favorable for cell attachment[17,18]. The successful fabrication and surface modification were also confirmed by XRD and FTIR tests. As shown in Figure 2C, the characteristic diffraction peaks of standard β-TCP (JCPDS09-169) were observed in eβP. In addition to the typical absorption spectrum of PDMS (1260 cm^{-1} for Si-CH$_3$, 1085 cm^{-1} for SI-O, 1015 cm^{-1} for Si-C, and 800 cm^{-1} for -CH$_3$), the distinct broad absorption band at 3377 cm^{-1} related to the N-H stretching vibration of PDA was found in eβP in Figure 2D and Figure S2.

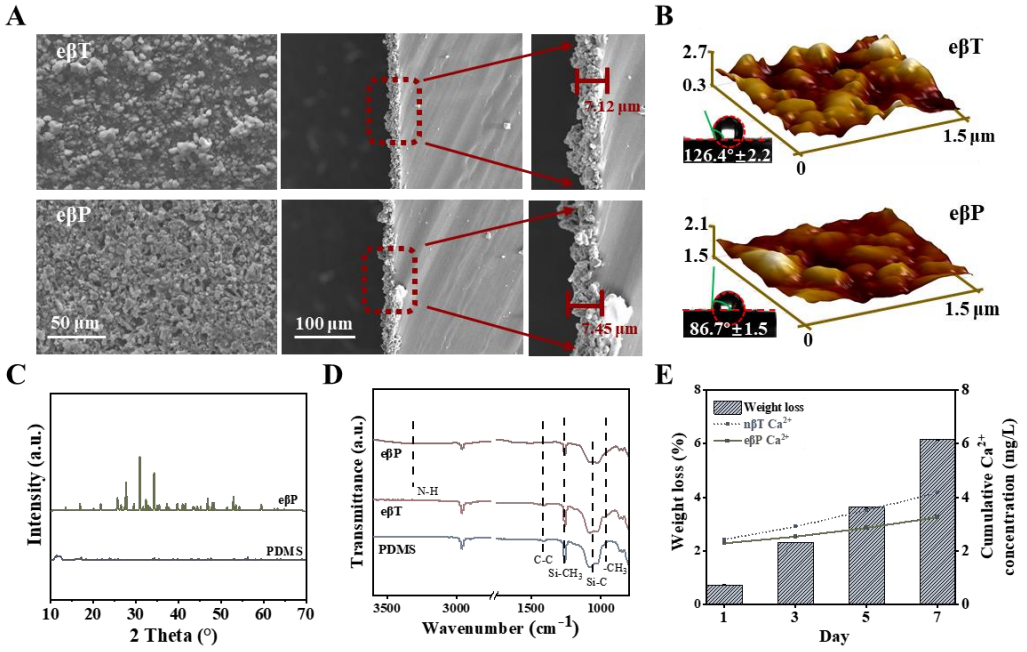

Figure 2. Characterization of eβP. (A) The SEM morphological characterizations of eβT and eβP. (B) AFM and water contact angle images of the samples. (C) XRD patterns in the range of 10-70°. (D) FTIR spectra of samples in the field of 4000-650 cm^{-1}. (E) Weight loss and released Ca^{2+} of nβT and eβP within 7 days.

Furthermore, the weight loss of the embedded nano-β-TCP in eβP over a 7-day period was obtained by gravimetric analysis in Figure 2E. The results revealed that the weight of eβP decreased slightly with time, and the mass of β-TCP decreased by 1.4 mg on the 7th day, which accounted for arround 6% of the total mass of β-TCP nanoparticles. Previous studies have reported no significant mass loss over a 7-day period for scaffolds made solely from sintered β-TCP nanoparticles[4]. Therefore, it was plausible that the weight loss observed in eβP could be primarily attributed to the release of a small amount of embedded nano-β-TCP from the sample surface. In addition, the release of Ca^{2+} from eβP compared to the nβT group (with 0.1 mg/mL nano-β-TCP in culture medium) was evaluated. As shown in Figure 2E, the Ca^{2+} concentrations in the solutions consistently increased over time. Specifically, the eβP exhibited slightly lower Ca^{2+} release than nβT. On day 7, the concentrations of Ca^{2+} released from eβP and nβT were 3.26±0.27 and 4.18±0.24 mg/L, respectively, which were within safe levels for cell viability as reported in other literature[19,20]. These results suggested that the nano-β-TCP integrated into eβP were gradually released from the surface, and the resulting concentration of Ca^{2+} was favorable for cell culture.

As shown in Figure S3, we measured the minimum complete peeling force of the coating to be 0.65 N by the material adhesion peeling experiment. Coefficient of friction (COF) is an important indicator for evaluating the tribological properties of coatings, and Figure S3 shows the time-varying COF variation of β-TCP semi-embedded coatings under 10 N sliding for 20 minutes. COF appeared to increase rapidly at the beginning of the tribological test and then to remain stable, with an average COF of 0.122 for eβP.

SEM characterization of eβP samples before and after stretching was performed in Figure S3, in which a small number of microcracks were present in the SeβP group, possibly resulting from nanoparticle shedding due to cyclic stretching loading. The Ca and P ions released by SeβP are shown in Figure S3. The contents of Ca and P in SeβP group were higher than those in eβP group, but there was no significant difference. All these show that the β-TCP semi-embedded layer and PDMS have a strong binding force.

3.2 Evaluation of Cell Adhesion and Proliferation on eβP Membrane

When cells were inoculated onto the modified films with different β-TCP contents, there was no significant difference in the survival rate and CCK-8 proliferation rate of cells in each group, as shown in Figure S4. Then, MSCs were cultured individually with PDMS, nβT, and eβP as shown in Figure 3A. Cell viability in live/dead staining in Figure 3B suggested that the ratios of living cells were more than 99% in all groups, indicating that the materials used in the experiment have no obvious toxic effects. In addition, the CCK-8 assay demonstrated that the optical density value values of cell proliferation activity in the culture plate were 0.50±0.03, 0.92±0.03, 1.46±0.05, and 2.04±0.03 on days 1, 3, 5, and 7, respectively, which was similar with cells cultured on PDMS. Compared to the PDMS group in Figure 3C, the proliferation rates in nβT and eβP groups on day 1 were significantly decreased to 48.3% and 62.1%, respectively. However, as time increased the cell proliferation rates pushed and tended to increase consistently, reaching 65.0% for nβT and 85.1% for eβP on day 7. The conclusion was further confirmed by EdU experiments (Figures 3D, E), which indicated that free nano-β-TCP could significantly inhibit the proliferation of MSCs compared to PDMS group. However, embedding nano-β-TCP on the surface of the material could obviously improve cell proliferation capability. According to the literature, the primary reason for the inhibitory effect of MSCs proliferation by nano-β-TCP may be the entry of free particles into the lysosomes which causes lysosomal rupture[21]. Therefore, we speculated the enhanced cell proliferation observed in the eβP group could attributed to the reduced release of free nano-β-TCP in the vicinity. In addition, the increased surface roughness of eβP may also promote the adhesion and proliferation of MSCs[22,23].

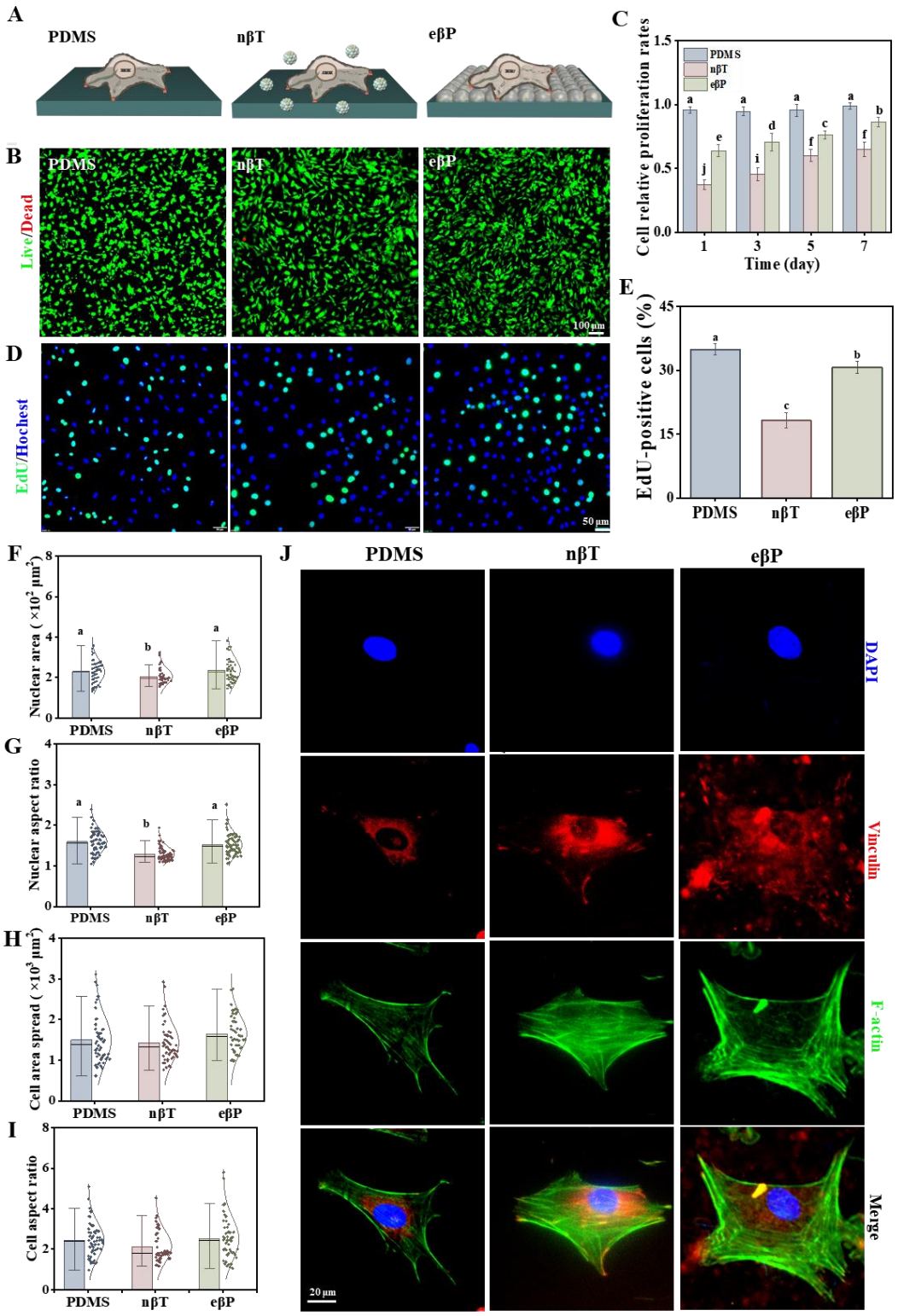

Figure 3. Behaviors of MSCs. (A) The schematic of cell adhesion on the PDMS, nβT and eβP groups. (B) Live/dead staining of cells in different groups. (C) The cell proliferation rates tested by CCK-8 assay. (D) Representative fluorescence images of EdU-positive cells in different groups. (E) Quantitative analysis of EdU cell proliferation assay. The statistical plots of data on (F) nuclear area , (G) nuclear aspect ratio, (H) cell area and (I) cell aspect ratio. (J) Fluorescence microscopy images with staining of F-actin, Vinculin, and DAPI.

Furthermore, the cytoskeletal morphology and focal adhesions (FAs) staining were analyzed after 24 h of cell culture among these groups, and no significant difference was detected in the aspect ratio and area of cells and nuclear between the PDMS and eβP groups, as shown in Figure 3F-I. However, the aspect ratio and area of nuclear in the nβT group were decreased compared to the other two groups, suggesting that nanoparticles may contribute to nuclear loss while being transported to the nuclear[24]. Noticeably, MSCs on eβP were enriched with FAs and exhibited polygonal morphology with the most pronounced filopodia (Figure 3J). This phenomenon may be attributed to the formation of a rough and inhomogeneous surface by nanoparticles on the eβP membrane[25]. Another possible explanation was that the hydrophilic modification caused by PDA could enhance MSCs spreading and adhesion[18]. As reported in the literature that the enriched FAs and cytoskeletal organization were closely related to the osteogenic activity of MSCs[26–28], we hypothesized that the roughness and hydrophilic surface of eβP films with a semi-embedded structure may favor MSCs osteogenic differentiation.

3.3 Dynamic Behaviors of MSCs on eβP Under UCS

Dynamic behaviors of MSCs cultured individually with PDMS, nβT, and eβP under ucs (1 Hz, 10% strain) were further investigated (Figure 4A). Compared with the EdU results under static conditions in Figure 3E, the cell proliferation rates on SPDMS, SnβT and SeβP decreased to 58.7%, 67.9% and 50.5%, respectively (Figure 4B, C), which could be attributed to mechanical stimulation[10,29]. Mechanical signals are transmitted through the cytoskeleton to the nuclear, inducing deformation of chromatin and altering transcription factor activity, thereby inhibiting cell proliferation[30,31]. Specifically, cell proliferation was higher in SeβP compared to SnβT possibly due to the fact that cells on SeβP exhibited stronger FAs (Figure 3J), which could allow cells to better resist contraction during stretching and produce greater tension in the cytoskeleton, ultimately reducing the compression of chromatin and the subsequent reduction of DNA synthesis[32].

Furthermore, dynamic cell adhesion after stretching was visualized as shown in Figure 4D (green for cytoskeleton and blue for nuclear), cells in all groups displayed a rounded shape immediately after mechanical stimulation (0 h). In Figure 4E, the skeleton contracted tightly around the nuclear, and the cell area in SPDMS and SnβT groups decreased dramatically to 334.8±116.9 and 376.4±170.1 μm^2. In comparison, the cell area in SeβP group was significantly higher, reaching 624.1±241.2 μm^2. After 24 h of recovery, the cell spread again on these materials and achieved a spreading area of 1513.5±512.9, 1245.1±512.8 and 1557.6±691.6 μm^2 for SPDMS, SnβT and SeβP groups, respectively. Specifically, cells in SPDMS were observed to have similar spreading area compared to those in the PDMS group. Conversely, the cell spreading area in the SnβT group was slightly reduced, while those in the SeβP group moderately enhanced, compared to their respective groups that were not subjected to stretching. Similarly, in Figure 4F, after mechanical stimulation, the nuclear area of each group decreased first and then recovered. The nuclear area of cells in SPDMS, SnβT, and SeβP groups after mechanical stimulation (0 h) decreased to 74.4%, 76.6%, and 80.0% compared to corresponding groups of PDMS, nβT, eβP, respectively. After 24 h, the

nuclear area on SPDMS, SnβT, and SeβP cells recovered to 240.5±59.4, 203.4±62.0 and 250.6±66.8 μm^2, respectively, which slightly increased compared to that of the unstretched groups in Figure 3G. Additionally, the nuclear aspect ratios of cells in SPDMS, SnβT, and SeβP groups (Figure S5) were similar to those in unstretched groups (Figure 3G), while the cellular aspect ratio (Figure S5) slightly increased compared with that of the corresponding unstretched group (Figure 3I).

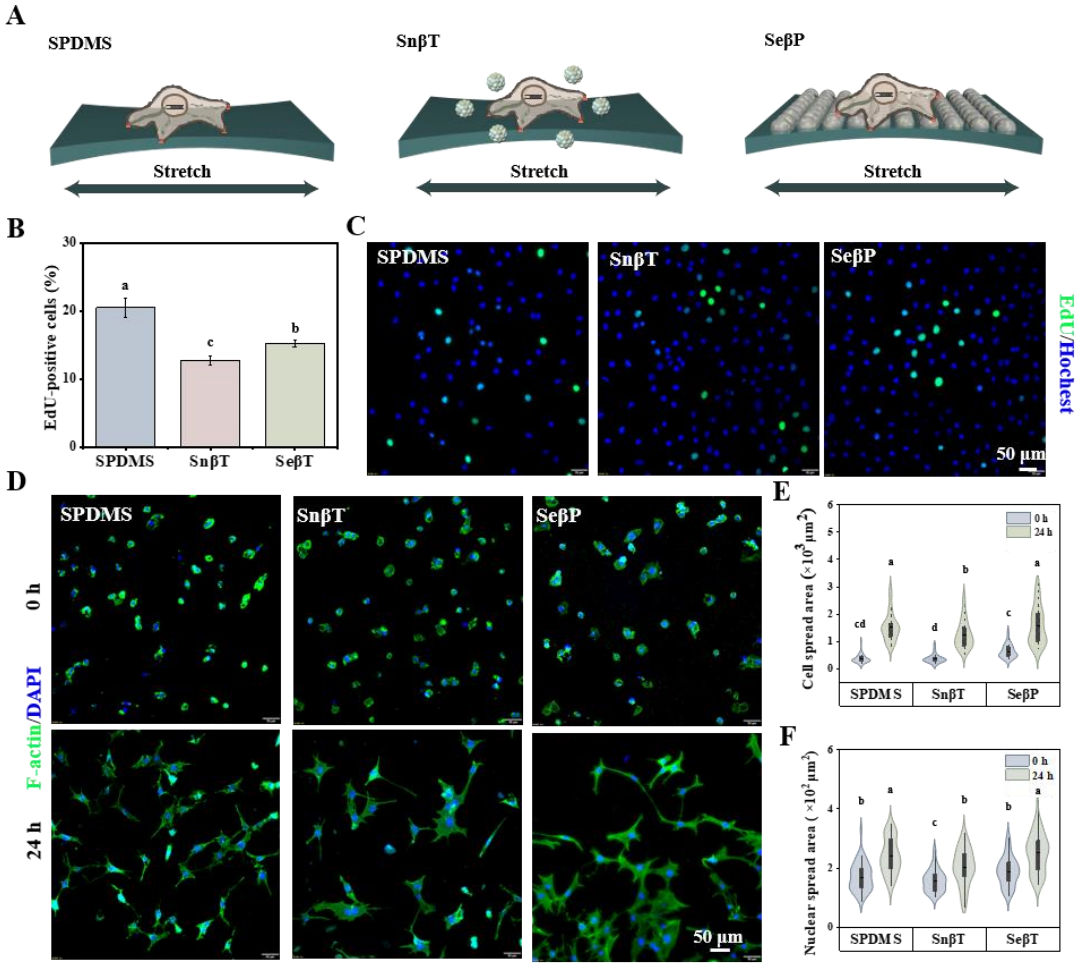

Figure 4. Behaviors of MSCs under UCS. (A) The schematic of cell cultured in SPDMS, SnβT and SeβP groups. (B) Quantitative analysis of EdU cell proliferation assay. (C) Representative fluorescence images of EdU-positive cells in different groups. (D) Cytoskeletal morphology after 0 h and 24 h recovery from UCS. Quantitative analysis of (E) cell spread area, and (F) nuclear spread area.

The changes in cell and nuclear morphology at 0 h may be due to mechanical stretching that increases intracellular calcium concentration, leading to cell contraction[33]. Furthermore, F-actin may mediate nuclear contraction by physical restriction at high load to provide protection against stretch-induced DNA damage, resulting in reduced nuclear area and increased chromatin compaction thereby affecting cell adhesion, proliferation, differentiation and other behaviors[34,35]. The recovery of cellular and nuclear area after 24 h was probably due to the subsequent spontaneous relaxation of the cells after cessation of dynamic stretching, which elongated the cells

and stabilized their adhesion to the extracellular matrix, allowing the cells to re-propagate[9]. However, the cells and nuclear in the SeβP group had slightly higher areas than the other two groups. This may be due to the surface nanostructures of eβP films and dopamine auto installation increasing the cellular FAs, thus making the cytoskeletal tension stronger and thus resisting cellular, nuclear contraction.

3.4 Osteogenic Differentiation of MSCs on eβP Membrane

Many publications have shown that MSCs' polygonal morphological distribution and the inhibition of cell proliferation were associated with MSCs' osteogenic differentiation[10]. To elucidate the mechanism of osteoinduction mediated by mechanical and chemical coupling, we first investigated the osteogenic differentiation of MSCs in different groups, while culturing MSCs on PDMS with the presence of osteogenic induction medium as the positive control (PDMS+ group). Typical bone formation markers BMP2 (a member of the Transforming growth factor beta (TGF-β) superfamily, and a growth factor that plays a key role in bone formation[36]) and RUNX2 (the RUNT-associated transcription factor 2, which plays a central role in osteoblast differentiation by binding to specific DNA sequences[37,38]) were stained and imaged. Results in Figure 5 showed that there was a significant difference in the expression of BMP2 and Runx2 between PDMS and PDMS+. In addition, the expression of BMP2 and Runx2 increased gradually in the following sequences: PDMS, PDMS+, nβT, SnβT, eβP, SeβP. While the expression of BMP2 in SeβP group was significantly higher than that in other groups, the expressions of RUNX2 in the SnβT, eβP, and SeβP groups were not significantly different. These results indicated that stem cells in SeβP group could be positively regulated toward osteogenic differentiation .

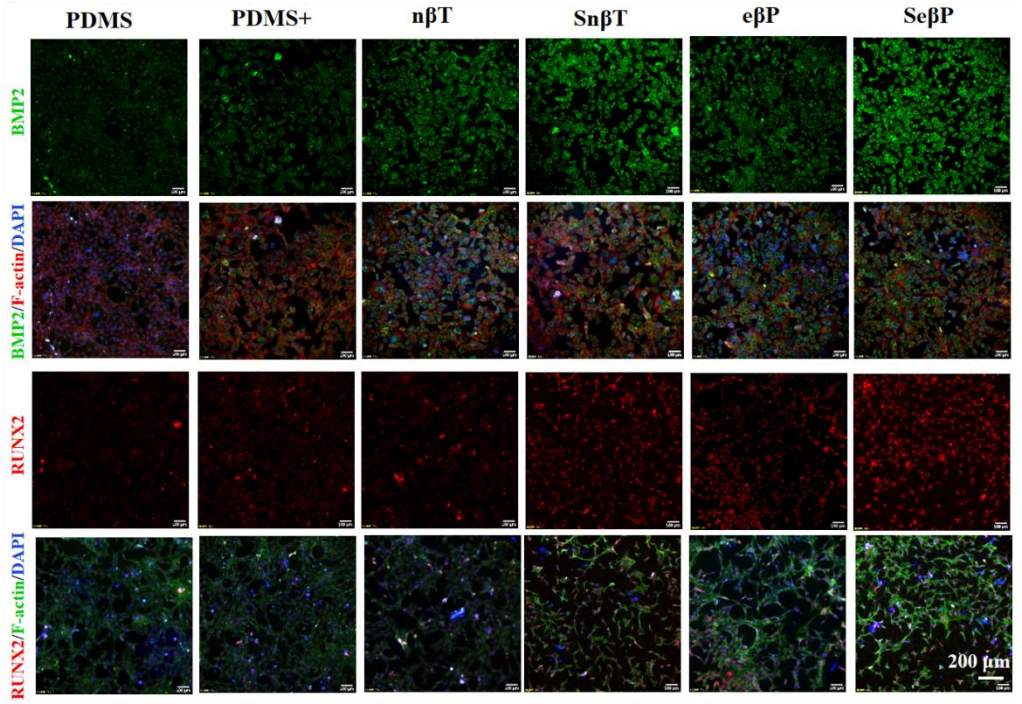

Figure 5. BMP2 and RUNX2 staining after culture for 3 days in different groups.

In addition, ALP staining and ARS were performed on MSCs cultured separately in PDMS, nβT, eβP, SnβT, and SeβP for 8 days. As shown in Figure 6A and B, the PDMS group did not show obvious signs of osteogenic differentiation within 4 days. Starting

on day 6, a visible purple staining reaction for ALP was observed, and ARS staining could be clearly distinguished as pink. By day 8, there was expansion in the ALP staining area, and an increase in the intensity of pink color was observed in ARS with a corresponding expansion in the staining area. Furthermore, expression of ALP for 8 days and OCN for 14 days were analyzed with the positive control group (PDMS+). As shown in Figure S6, cells in SeβP group displayed highest osteogenic differentiation.

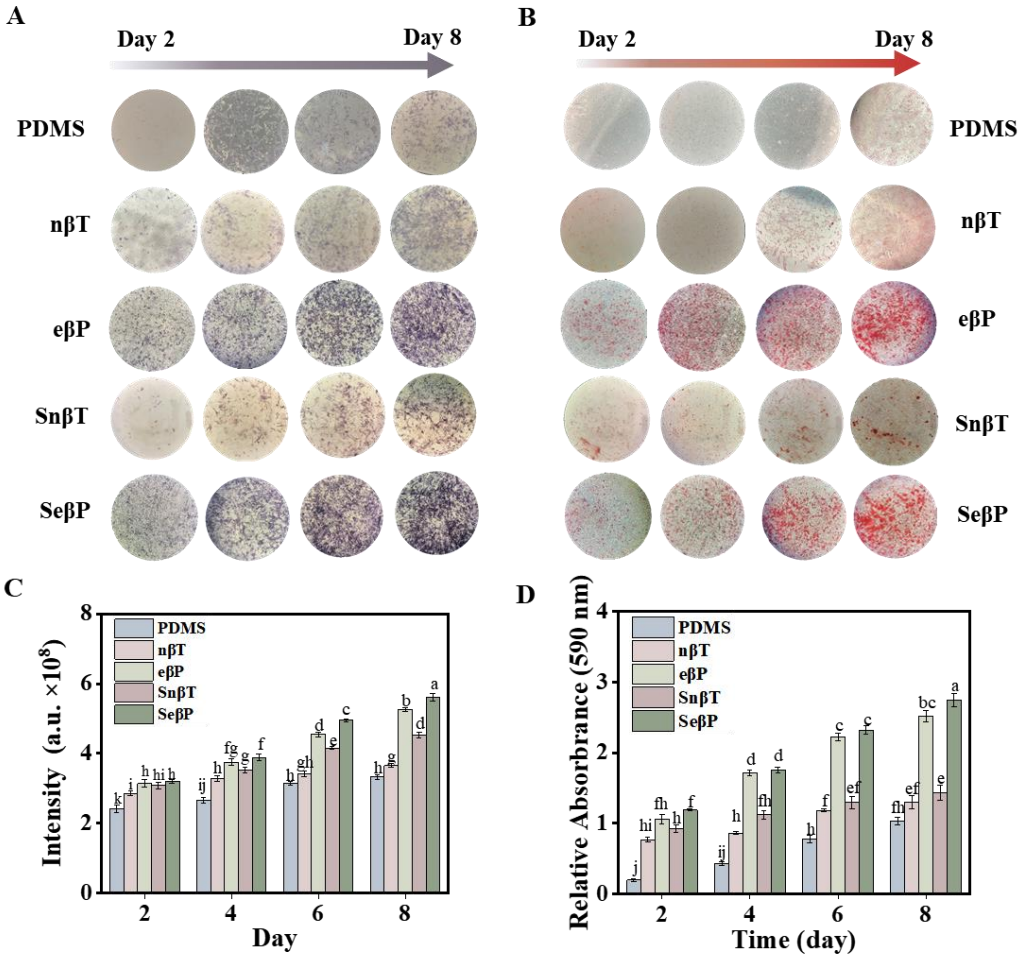

Figure 6. Osteogenic differentiation of MSCs cultured in different groups. (A) ALP staining and (B) ARS of cells after cultured for 2, 4, 6, 8 days. (C) Quantitative analysis of ALP activity and (D) ARS mineral deposition.

These data suggest that β-TCP has an excellent ability to promote osteogenic differentiation, which was consistent with literature reports[39,40]. In particular, the semi-embedded structure proposed in the study was more favorable for osteogenic differentiation compared to free nano-β-TCP. The possible reason was that the semi-embedded structure reduces the entry of nano-β-TCP into lysosomes, which may cause damage to lysosomes, mitochondria and other organelles[20]. Additionally, mechanical stimulation seems to further improve osteogenic differentiation of MSCs. Semiquantitative results manifested that SnβT and SeβP groups exhibited slightly enhanced BMP2 and RUNX2 after culture for 3 days, and significantly higher ALP and ARS compared to their respective group (nβT and eβP) that did not receive tensile

loading. This could be attributed to the possibility that the cells stored the stimulus information internally after stretching, which allowed for continuous gene expression over an extended period, ultimately leading to a more notable inclination towards osteogenic differentiation[11,41]. Specifically, SeβP showed the strongest ability to induce osteogenic differentiation of MSCs. Considering the previous proliferation tests (Figure 4B and C), we concluded that stretch stimulation may impede cell proliferation by promoting the differentiation ability of MSCs.

3.5 *In vitro* Regulation of Osteogenic Differentiation by SeβP

To delve deeper into the regulation mechanism of cell differentiation on eβP membrane, the RT-qPCR assay was implemented to verify expression levels of mechanical transduction markers such as Piezo-type mechanosensitive ion channel component 1 (*Piezo1*), calcium-related markers Calmodulin (*Cam*) and Calcium/calmodulin-dependent protein kinase II (*Camk2*), and osteogenic differentiation markers *Alp*, Collagen type I (C*ol1a*), *Runx2*, *Bmp2*. As shown in Figure 7A, the expression of *Cam* and *Camk2* genes were upregulated in nβT and eβP groups as compared to the PDMS group, indicating the activation of the calcium signaling pathway caused by Ca^{2+} release from β-TCP. While the expression of *Piezo1* was comparable between the PDMS and nβT groups, the levels of *Piezo1* significantly upregulated by 3 times in the eβP group, suggesting that morphological change induced by nano-β-TCP embedding could activate the mechanical transduction pathway, which would further enhance *Cam* expression. Additionally, compared to static conditions, mechanical stretch could enhance the expression of *Piezo1* in MSCs. The synchronization of surface roughness and stretching resulted in 4 times higher expression of *Piezo1* in the eβP group compared to the PDMS group, which led to the upregulation of *Cam* and *Camk2* genes.

Furthermore, the expression levels of osteogenic differentiation genes (*Alp*, *Col1a*, *Bmp2* and *Runx2*) were significantly increased in nβT and eβP groups as compared to the PDMS group in Figure 7A, indicating that the activation of the calcium signaling pathway could positively affect the osteogenic differentiation of MSCs through all of the typical markers discussed in the study. Specifically, the expression of *Alp* and *Col1a* showed a gradual increase in the following sequence of groups: PDMS, nβT, eβP, SnβT, and SeβP. However, the expression of *Bmp2* and *Runx2* were higher in eβP than those in PDMS, nβT and SnβT, and highest in SeβP, showing a similar trend as the expression of *Piezo1* in these groups in Figure 7A. These results indicated that the calcium signaling pathway and mechanical transduction pathway were both activated in SeβP to regulate cell differentiation, and the activation of PIEZO1 could specifically contribute to the expression of its downstream genes *Bmp2* and *Runx2*.

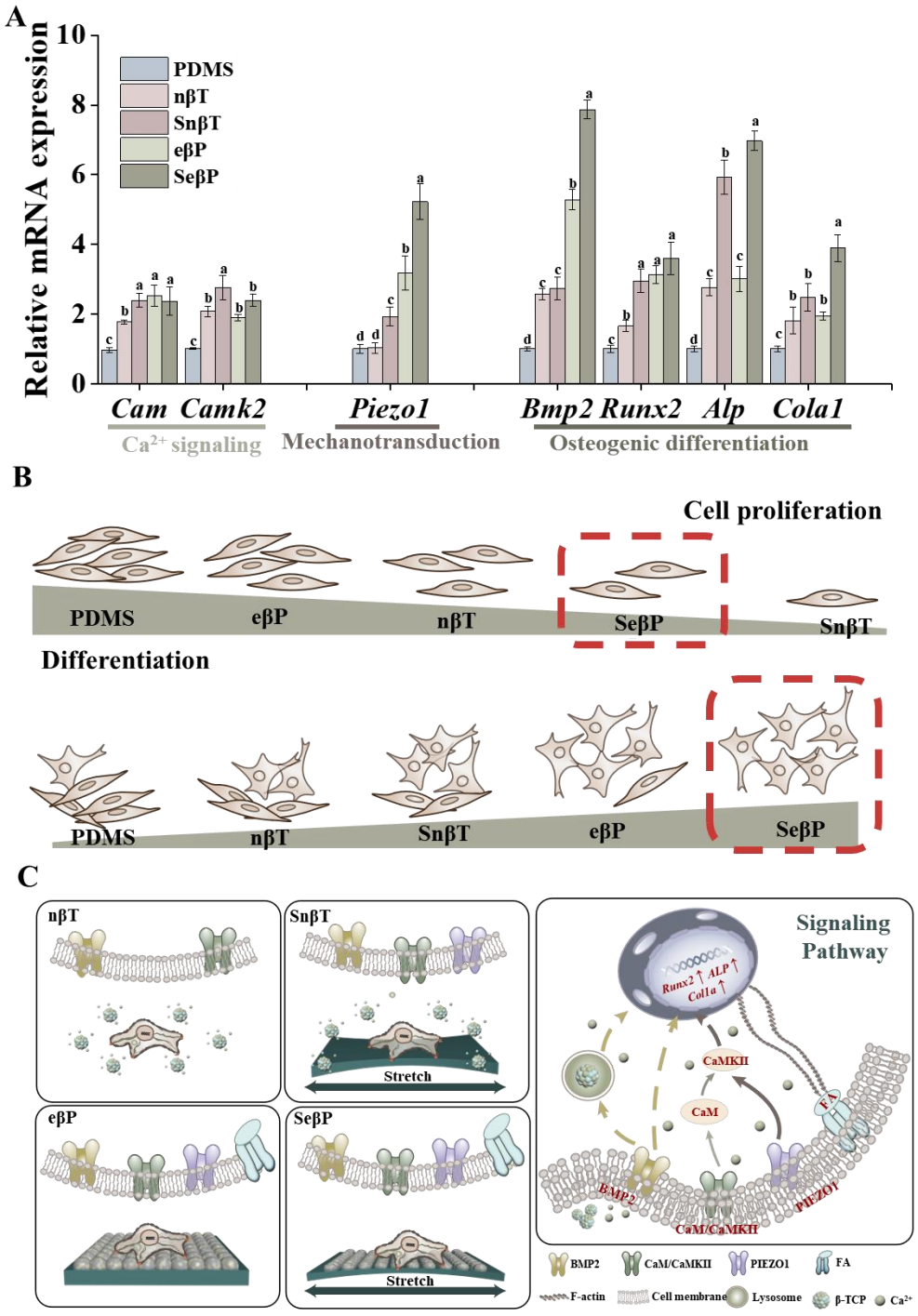

Figure 7. Regulation of Osteogenic Differentiation by SeβP. (A) Relative expression of genes in PDMS, nβT, eβP, SnβT and SeβP groups. (B) The schematic illustration of cell proliferation and differentiation in different groups. (C)The schematic illustration of the postulated cell regulation mechanisms.

By grouping PDMS, nβT, eβP, SnβT, and SeβP, we simultaneously explored the effects on MSCs proliferation and differentiation under the chemical factors and mechanical stimulation. The schematic comparison of the proliferation and

differentiation ability of MSCs is shown in Figure 7B. It was noteworthy that regardless of the presence of UCS, semi-embedded films exhibited a superior capacity in stimulating cell proliferation and promoting osteogenic differentiation when compared to free nano-β-TCP, suggesting that the semi-embedded structure served as a more effective strategy in bone tissue engineering. This may be due to, (1) the semi-embedded structure provided a mechanical cue to improve the stem cell microenvironment through moderate roughness, which positively regulated cell behavior. (2) the semi-embedded structure reduced the entry of nanoparticles into lysosomes leading to lysosome rupture and damage to cells, which improved the cell proliferation microenvironment.

Furthermore, we decoupled the effects of chemical and mechanical stimuli in cell osteogenic differentiation (schematically illustrated in Figure 7C). Previous studies have shown that β-TCP induced changes in calcium concentrations, allowing the activation of the Cam-camkII pathways[42,43]. In addition, β-TCP can enter the cell through endocytosis and phosphorylate the protein SMAD1/5/8, which triggers the BMP2/SMAD/RUNX2 signaling pathway. SMAD1/5/8 forms a complex with SMAD 4 and enters the nuclear, regulating cell proliferation and differentiation capacity as a transcription factor[44,45]. Our study was consistence with these findings. Significantly, our experimental results showed that surface roughness caused by nanoparticle embedding and hydrophilic modification by PDA enhanced the adhesion of MSCs, forming FAs aggregation, and effectively induced PIEZO1 channel opening, which positively regulated the osteogenic differentiation of cells. Furthermore, under a dynamic microenvironment of tensile loading, the expression of *Piezo1* could be further enhanced. Kenmochi et al. have reported similar results that UCS can efficiently induce PIEZO1 channel opening, which in turn triggers the BMP2/SMAD signaling pathway, increasing *Runx2* and *Bmp2* levels[46]. Our results proved that while chemical and mechanical stimulation simultaneously exist, they have the ability to collaborate in facilitating osteogenic differentiation. The neoteric semi-embedded structure proposed in the study was proved as a valuable strategy to enable the formation of sustainable ion exchange and promote the process of bone repair.

4. Conclusion

A facile and reliable method was proposed to form semi-embedded β-TCP nanoparticles on elastic polymer, enabling sustainable Ca^{2+} release and fostering cell regulation in static and dynamic culture conditions. The thorough characterization of the morphology, roughness and weight of the material demonstrated that eβP could contribute to a rough surface and gradually release of Ca^{2+}, which were favorable for cell culture. Specifically, the Ca^{2+} in the environment effectively activated the calcium signaling pathway of MSCs, and the roughness increased intracellular FAs aggregation and the cell spreading, contributing to the opening of the PIEZO1 signaling pathway. Under the dynamic condition of UCS (10% strain, 1 Hz), the expression of *Piezo1* in MSCs could be further enhanced, synergistically promoting osteogenic differentiation of cells. While both of the chemical and mechanical stimuli could obviously upregulate typical markers, including *Alp, Col1a*, *Runx2*, and *Bmp2*, the activation of the piezo1

signaling pathway exhibited a more important role in regulating *Runx2* and *Bmp2* genes. These findings effectively decoupled the roles of the chemical stimuli, the roughness and the dynamic tensile strain in proliferation and osteogenic differentiation of MSCs, elucidating the effectiveness of eβP as a novel strategy for cell regulation. In addition, the semi-embedded strategy could be extended to more other biomaterials optimization designs containing nanoparticles and polymers, which is valuable for various biomedical applications.

Supporting Information

Characterization of β-TCP (Figure S1). (A) The SEM image–(B) The EDS map showing detection of calcium (red) and phosphorus (green). (C) EDS spectrum of elemental content. (D) XRD patterns in the rage of 10-70° (Figure S2). Stability of eβP (Figure S3). (A) Schematic diagram of adhesion peeling test. (B) COF of the coating with time at 10 N. (C) The SEM morphological characterizations of eβP and SeβP. (D) Released Ca and P of eβP and SeβP. Biocompatibility of MSCs (Figure S4). (A) Live/dead staining of cells in different groups. (B) cell survival rate. (C) The cell proliferation rates tested by CCK-8 assay. Figure S5 (A) nuclear and (B) cell aspect ratio after 24 h of recovery from stretching. ALP staining and ARS of cells after cultured for 7 or 14 days (Figure S6).

Corresponding Author

* Corresponding author. Institute of Biomedical Engineering, College of Medicine, Key Laboratory of Advanced Technologies of Materials, Ministry of Education, School of Materials Science and Engineering, Southwest Jiaotong University, Chengdu 610031, P.R. China. Phone: +86-18380201248.

e-mail address: xgou@swjtu.edu.cn

Author Contributions

Yujie Dai: Investigation, visualization, writing – original draft. **Qingyun Xie:** Methodology, investigation, Writing. **Yimeng Zhang:** Methodology, investigation. **Yiwan Sun:** Investigation,Validation. **Shaomei Zhu:** Software, investigation. **Chongyu Wang:** Software, investigation. **Youhua Tan:** Methodology, writing – review & editing. **Xue Gou:** Supervision, methodology, writing – review & editing.

Acknowledgments

This work was supported by the National Natural Science Foundation of China (12002292), the New Interdisciplinary Cultivation Funds of Southwest Jiaotong University (2682023JX005), Sichuan Science and Technology Program (2022YFG0365), and the Postgraduate Education and Teaching Reform Project of SWJTU (YJG52022Y019). We also thank the Analysis and Testing Center of Southwest Jiaotong University for the SEM tests.

Notes

The authors declare no competing financial interest.

Reference

(1) Cross, L. M.; Thakur, A.; Jalili, N. A.; Detamore, M.; Gaharwar, A. K. Nanoengineered Biomaterials for Repair and Regeneration of Orthopedic Tissue Interfaces. *Acta Biomater.* **2016**, *42*, 2–17. https://doi.org/10.1016/j.actbio.2016.06.023.

(2) Lu, H.; Zhou, Y.; Ma, Y.; Xiao, L.; Ji, W.; Zhang, Y.; Wang, X. Current Application of Beta-Tricalcium Phosphate in Bone Repair and Its Mechanism to Regulate Osteogenesis. *Front. Mater.* **2021**, *8*, 698915. https://doi.org/10.3389/fmats.2021.698915.

(3) Bohner, M.; Santoni, B. L. G.; Döbelin, N. β-Tricalcium Phosphate for Bone Substitution: Synthesis and Properties. *Acta Biomater.* **2020**, *113*, 23–41. https://doi.org/10.1016/j.actbio.2020.06.022.

(4) Feng, P.; Wu, P.; Gao, C.; Yang, Y.; Guo, W.; Yang, W.; Shuai, C. A Multimaterial Scaffold With Tunable Properties: Toward Bone Tissue Repair. *Adv. Sci.* **2018**, *5* (6), 1700817. https://doi.org/10.1002/advs.201700817.

(5) Dienel, K. E. G.; van Bochove, B.; Seppälä, J. V. Decoupling the Role of Chemistry and Microstructure in hMSCs Response to an Osteoinductive Calcium Phosphate Ceramic. *Bioact. Mater.* **2023**, *19* (2), 127–138. https://doi.org/10.1021/acs.biomac.9b01272.

(6) Petrovic, L.; Pohle, D.; Münstedt, H.; Rechtenwald, T.; Schlegel, K. A.; Rupprecht, S. Effect of βTCP Filled Polyetheretherketone on Osteoblast Cell Proliferationin Vitro. *J. Biomed. Sci.* **2006**, *13* (1), 41–46. https://doi.org/10.1007/s11373-005-9032-z.

(7) Qiao, D.; Zhang, T.; Tang, M. Autophagy Regulation by Inorganic, Organic, and Organic/Inorganic Hybrid Nanoparticles: Organelle Damage, Regulation Factors, and Potential Pathways. *J. Biochem. Mol. Toxicol.* **1970**, *n/a* (n/a), e23429. https://doi.org/10.1002/jbt.23429.

(8) Jo, J.; Abdi Nansa, S.; Kim, D.-H. Molecular Regulators of Cellular Mechanoadaptation at Cell–Material Interfaces. *Front. Bioeng. Biotechnol.* **2020**, *8*. https://doi.org/10.3389/fbioe.2020.608569.

(9) Wu, Z.; Wong, K.; Glogauer, M.; Ellen, R. P.; McCulloch, C. A. G. Regulation of Stretch-Activated Intracellular Calcium Transients by Actin Filaments. *Biochem. Biophys. Res. Commun.* **1999**, *261* (2), 419–425. https://doi.org/10.1006/bbrc.1999.1057.

(10) Carroll, S. F.; Buckley, C. T.; Kelly, D. J. Cyclic Tensile Strain Can Play a Role in Directing Both Intramembranous and Endochondral Ossification of Mesenchymal Stem Cells. *Front. Bioeng. Biotechnol.* **2017**, *5*, 73. https://doi.org/10.3389/fbioe.2017.00073.

(11) Wei, D.; Liu, A.; Sun, J.; Chen, S.; Wu, C.; Zhu, H.; Chen, Y.; Luo, H.; Fan, H. Mechanics-Controlled Dynamic Cell Niches Guided Osteogenic Differentiation of Stem Cells via Preserved Cellular Mechanical Memory. *ACS Appl. Mater. Amp Interfaces* **2020**, *12* (1), 260–274. https://doi.org/10.1021/acsami.9b18425.

(12) Choi, C. K. K.; Li, J.; Wei, K.; Xu, Y. J.; Ho, L. W. C.; Zhu, M.; To, K. K. W.; Choi, C. H. J.; Bian, L. A Gold@Polydopamine Core–Shell Nanoprobe for Long-Term Intracellular Detection of MicroRNAs in Differentiating Stem Cells. *J. Am. Chem. Soc.* **2015**, *137* (23), 7337–7346. https://doi.org/10.1021/jacs.5b01457.

(13) Xue, G.; Zhang, Y.; Xie, T.; Zhang, Z.; Liu, Q.; Li, X.; Gou, X. Cell Adhesion-Mediated Piezoelectric Self-Stimulation on Polydopamine-Modified Poly(Vinylidene Fluoride) Membranes.

ACS Appl. Mater. Amp Interfaces **2021**, *13* (15), 17361–17371. https://doi.org/10.1021/acsami.1c02457.
(14) Kuruba, M.; Gaikwad, G.; Natarajan, J.; Koppad, P. G. Effect of Carbon Nanotubes on Microhardness and Adhesion Strength of High-Velocity Oxy-Fuel Sprayed NiCr–Cr_3C_2 Coatings. *Proc. Inst. Mech. Eng. Part J. Mater. Des. Appl.* **2022**, *236* (1), 86–96. https://doi.org/10.1177/14644207211040922.
(15) Meng, L.; Xue, G.; Liu, Q.; Xie, T.; Fan, D.; Gou, X. In-Situ Electromechanical Testing and Loading System for Dynamic Cell-Biomaterial Interaction Study. *Biomed. Microdevices* **2020**, *22* (3), 56. https://doi.org/10.1007/s10544-020-00514-3.
(16) Zhou, J.; Gou, X.; Fan, D.; Wang, J.; Wan, Z. Polydimethylsiloxane/$BaTiO_3$ Nanogenerators with a Surface-Assembled Mosaic Structure for Enhanced Piezoelectric Sensing. *ACS Appl. Mater. Interfaces* **2022**, *14* (33), 38105–38115. https://doi.org/10.1021/acsami.2c04196.
(17) Zhang, D.; Zheng, H.; Geng, K.; Shen, J.; Feng, X.; Xu, P.; Duan, Y.; Li, Y.; Wu, R.; Gou, Z.; Gao, C. Large Fuzzy Biodegradable Polyester Microspheres with Dopamine Deposition Enhance Cell Adhesion and Bone Regeneration in Vivo. *Biomaterials* **2021**, *272*, 120783. https://doi.org/10.1016/j.biomaterials.2021.120783.
(18) Wang, Z.; Chen, L.; Wang, Y.; Chen, X.; Zhang, P. Improved Cell Adhesion and Osteogenesis of Op-HA/PLGA Composite by Poly(Dopamine)-Assisted Immobilization of Collagen Mimetic Peptide and Osteogenic Growth Peptide. *ACS Appl. Mater. Amp Interfaces* **2016**, *8* (40), 26559–26569. https://doi.org/10.1021/acsami.6b08733.
(19) Gao, P.; Zhang, H.; Liu, Y.; Fan, B.; Li, X.; Xiao, X.; Lan, P.; Li, M.; Geng, L.; Liu, D.; Yuan, Y.; Lian, Q.; Lu, J.; Guo, Z.; Wang, Z. Beta-Tricalcium Phosphate Granules Improve Osteogenesis in Vitro and Establish Innovative Osteo-Regenerators for Bone Tissue Engineering in Vivo. *Sci. Rep.* **2016**, *6* (1), 23367. https://doi.org/10.1038/srep23367.
(20) Nakagawa, Y.; Muneta, T.; Tsuji, K.; Ichinose, S.; Hakamatsuka, Y.; Koga, H.; Sekiya, I. β-Tricalcium Phosphate Micron Particles Enhance Calcification of Human Mesenchymal Stem Cells In Vitro. *J. Nanomater.* **2013**, *2013*, e426786. https://doi.org/10.1155/2013/426786.
(21) Li, Y.; Hu, Q.; Miao, G.; Zhang, Q.; Yuan, B.; Zhu, Y.; Fu, X.; Chen, X.; Mao, C. Size-Dependent Mechanism of Intracellular Localization and Cytotoxicity of Mono-Disperse Spherical Mesoporous Nano- and Micron-Bioactive Glass Particles. *J. Biomed. Nanotechnol.* **2016**, *12* (5), 863–877. https://doi.org/10.1166/jbn.2016.2235.
(22) Gorodzha, S. N.; Muslimov, A. R.; Syromotina, D. S.; Timin, A. S.; Tcvetkov, N. Y.; Lepik, K. V.; Petrova, A. V.; Surmeneva, M. A.; Gorin, D. A.; Sukhorukov, G. B.; Surmenev, R. A. A Comparison Study between Electrospun Polycaprolactone and Piezoelectric Poly(3-Hydroxybutyrate-Co-3-Hydroxyvalerate) Scaffolds for Bone Tissue Engineering. *Colloids Surf. B Biointerfaces* **2017**, *160*, 48–59. https://doi.org/10.1016/j.colsurfb.2017.09.004.
(23) Andrukhov, O.; Huber, R.; Shi, B.; Berner, S.; Rausch-Fan, X.; Moritz, A.; Spencer, N. D.; Schedle, A. Proliferation, Behavior, and Differentiation of Osteoblasts on Surfaces of Different Microroughness. *Dent. Mater.* **2016**, *32* (11), 1374–1384. https://doi.org/10.1016/j.dental.2016.08.217.
(24) Dam, D. H. M.; Lee, J. H.; Sisco, P. N.; Co, D. T.; Zhang, M.; Wasielewski, M. R.; Odom, T. W. Direct Observation of Nanoparticle–Cancer Cell Nucleus Interactions. *ACS Nano* **2012**, *6* (4), 3318–3326. https://doi.org/10.1021/nn300296p.
(25) Hou, Y.; Xie, W.; Yu, L.; Camacho, L. C.; Nie, C.; Zhang, M.; Haag, R.; Wei, Q. Surface

Roughness Gradients Reveal Topography-Specific Mechanosensitive Responses in Human Mesenchymal Stem Cells. *Small* **2020**, *16* (10), 1905422. https://doi.org/10.1002/smll.201905422.
(26) Liu, W.; Wei, Y.; Zhang, X.; Xu, M.; Yang, X.; Deng, X. Lower Extent but Similar Rhythm of Osteogenic Behavior in hBMSCs Cultured on Nanofibrous Scaffolds *versus* Induced with Osteogenic Supplement. *ACS Nano* **2013**, *7* (8), 6928–6938. https://doi.org/10.1021/nn402118s.
(27) Yang, J.; McNamara, L. E.; Gadegaard, N.; Alakpa, E. V.; Burgess, K. V.; Meek, R. M. D.; Dalby, M. J. Nanotopographical Induction of Osteogenesis through Adhesion, Bone Morphogenic Protein Cosignaling, and Regulation of MicroRNAs. *ACS Nano* **2014**, *8* (10), 9941–9953. https://doi.org/10.1021/nn504767g.
(28) Guo, Y.; Yan, R.; Wang, X.; Liang, G.; Yang, A.; Li, J. Near-Infrared Light-Controlled Activation of Adhesive Peptides Regulates Cell Adhesion and Multidifferentiation in Mesenchymal Stem Cells on an Up-Conversion Substrate. *Nano Lett.* **2022**, *22* (6), 2293–2302. https://doi.org/10.1021/acs.nanolett.1c04534.
(29) Sun, K.; Liu, F.; Wang, J.; Guo, Z.; Ji, Z.; Yao, M. The Effect of Mechanical Stretch Stress on the Differentiation and Apoptosis of Human Growth Plate Chondrocytes. *Vitro Cell. Dev. Biol. - Anim.* **2017**, *53* (2), 141–148. https://doi.org/10.1007/s11626-016-0090-5.
(30) Zhang, D.; Zhang, R.; Song, X.; Yan, K. C.; Liang, H. Uniaxial Cyclic Stretching Promotes Chromatin Accessibility of Gene Loci Associated With Mesenchymal Stem Cells Morphogenesis and Osteogenesis. *Front. Cell Dev. Biol.* **2021**, *9*, 664545. https://doi.org/10.3389/fcell.2021.664545.
(31) Heo, S.-J.; Han, W. M.; Szczesny, S. E.; Cosgrove, B. D.; Elliott, D. M.; Lee, D. A.; Duncan, R. L.; Mauck, R. L. Mechanically Induced Chromatin Condensation Requires Cellular Contractility in Mesenchymal Stem Cells. *Biophys. J.* **2016**, *111* (4), 864–874. https://doi.org/10.1016/j.bpj.2016.07.006.
(32) Kirby, T. J.; Lammerding, J. Emerging Views of the Nucleus as a Cellular Mechanosensor. *Nat. Cell Biol.* **2018**, *20* (4), 373–381. https://doi.org/10.1038/s41556-018-0038-y.
(33) Chubinskiy-Nadezhdin, V. I.; Vasileva, V. Y.; Pugovkina, N. A.; Vassilieva, I. O.; Morachevskaya, E. A.; Nikolsky, N. N.; Negulyaev, Y. A. Local Calcium Signalling Is Mediated by Mechanosensitive Ion Channels in Mesenchymal Stem Cells. *Biochem. Biophys. Res. Commun.* **2017**, *482* (4), 563–568. https://doi.org/10.1016/j.bbrc.2016.11.074.
(34) Seelbinder, B. TENSCell: Imaging of Stretch-Activated Cells Reveals Divergent Nuclear Behavior and Tension. *Biophys. J.* **2020**, *118* (11), 2627–2640. https://doi.org/10.1016/j.bpj.2020.03.035.
(35) Alisafaei, F.; Jokhun, D. S.; Shivashankar, G. V.; Shenoy, V. B. Regulation of Nuclear Architecture, Mechanics, and Nucleocytoplasmic Shuttling of Epigenetic Factors by Cell Geometric Constraints. *Proc. Natl. Acad. Sci.* **2019**, *116* (27), 13200–13209. https://doi.org/10.1073/pnas.1902035116.
(36) Jung, T.; Lee, J. H.; Park, S.; Kim, Y.-J.; Seo, J.; Shim, H.-E.; Kim, K.-S.; Jang, H.-S.; Chung, H.-M.; Oh, S.-G.; Moon, S.-H.; Kang, S.-W. Effect of BMP-2 Delivery Mode on Osteogenic Differentiation of Stem Cells. *Stem Cells Int.* **2017**, *2017*, 1–7. https://doi.org/10.1155/2017/7859184.
(37) Komori, T.; Yagi, H.; Nomura, S.; Yamaguchi, A.; Sasaki, K.; Deguchi, K.; Shimizu, Y.; Bronson, R. T.; Gao, Y.-H.; Inada, M.; Sato, M.; Okamoto, R.; Kitamura, Y.; Yoshiki, S.; Kishimoto, T. Targeted Disruption of Results in a Complete Lack of Bone Formation Owing to Maturational Arrest of Osteoblasts. *Cell* **1997**, *89* (5), 755–764. https://doi.org/10.1016/s0092-8674(00)80258-5.

(38) Ducy, P.; Zhang, R.; Geoffroy, V.; Ridall, A. L.; Karsenty, G. Osf2/Cbfa1: A Transcriptional Activator of Osteoblast Differentiation. *Cell* **1997**, *89* (5), 747–754. https://doi.org/10.1016/S0092-8674(00)80257-3.
(39) Zhuang, P.; Wu, X.; Dai, H.; Yao, Y.; Qiu, T.; Han, Y.; Li, S. Nano β-Tricalcium Phosphate/Hydrogel Encapsulated Scaffolds Promote Osteogenic Differentiation of Bone Marrow Stromal Cells through ATP Metabolism. *Mater. Amp Des.* **2021**, *208*, 109881. https://doi.org/10.1016/j.matdes.2021.109881.
(40) Liu, Y.; Ma, Y.; Zhang, J.; Xie, Q.; Wang, Z.; Yu, S.; Yuan, Y.; Liu, C. MBG-Modified β-TCP Scaffold Promotes Mesenchymal Stem Cells Adhesion and Osteogenic Differentiation via a FAK/MAPK Signaling Pathway. *ACS Appl. Mater. Amp Interfaces* **2017**, *9* (36), 30283–30296. https://doi.org/10.1021/acsami.7b02466.
(41) Yang, C.; Tibbitt, M. W.; Basta, L.; Anseth, K. S. Mechanical Memory and Dosing Influence Stem Cell Fate. *Nat. Mater.* **2014**, *13* (6), 645–652. https://doi.org/10.1038/nmat3889.
(42) Cary, R. L.; Waddell, S.; Racioppi, L.; Long, F.; Novack, D. V.; Voor, M. J.; Sankar, U. Inhibition of Ca^{2+} /Calmodulin–Dependent Protein Kinase Kinase 2 Stimulates Osteoblast Formation and Inhibits Osteoclast Differentiation. *J. Bone Miner. Res.* **2013**, *28* (7), 1599–1610. https://doi.org/10.1002/jbmr.1890.
(43) Liu, W.; Le, C. C.; Wang, D.; Ran, D.; Wang, Y.; Zhao, H.; Gu, J.; Zou, H.; Yuan, Y.; Bian, J.; Liu, Z. Ca2+/CaM/CaMK Signaling Is Involved in Cadmium-Induced Osteoclast Differentiation. *Toxicology* **2020**, *441*, 152520. https://doi.org/10.1016/j.tox.2020.152520.
(44) Paarmann, P.; Dörpholz, G.; Fiebig, J.; Amsalem, A. R.; Ehrlich, M.; Henis, Y. I.; Müller, T.; Knaus, P. Dynamin-Dependent Endocytosis of Bone Morphogenetic Protein2 (BMP2) and Its Receptors Is Dispensable for the Initiation of Smad Signaling. *Int. J. Biochem. Amp Cell Biol.* **2016**, *76*, 51–63. https://doi.org/10.1016/j.biocel.2016.04.010.
(45) Hegarty, S. V.; Sullivan, A. M.; O'Keeffe, G. W. Endocytosis Contributes to BMP2-Induced Smad Signalling and Neuronal Growth. *Neurosci. Lett.* **2017**, *643*, 32–37. https://doi.org/10.1016/j.neulet.2017.02.013.
(46) Wei, Q.; Holle, A.; Li, J.; Posa, F.; Biagioni, F.; Croci, O.; Benk, A. S.; Young, J.; Noureddine, F.; Deng, J.; Zhang, M.; Inman, G. J.; Spatz, J. P.; Campaner, S.; Cavalcanti-Adam, E. A. BMP-2 Signaling and Mechanotransduction Synergize to Drive Osteogenic Differentiation via YAP/TAZ. *Adv. Sci.* **2020**, *7* (15), 1902931. https://doi.org/10.1002/advs.201902931.